High-Throughput Area-Selective Spatial Atomic Layer Deposition of SiO₂ with Interleaved Small Molecule Inhibitors and Integrated Back-Etch Correction for Low Defectivity

Bora Karasulu, Fred Roozeboom,* and Alfredo Mameli**

A first-of-its-kind area-selective deposition process for SiO₂ is developed consisting of film deposition with interleaved exposures to small molecule inhibitors (SMIs) and back-etch correction steps, within the same spatial atomic layer deposition (ALD) tool. The synergy of these aspects results in selective SiO₂ deposition up to ~23 nm with high selectivity and throughput, with SiO₂ growth area and ZnO nongrowth area. The selectivity is corroborated by both X-ray photoelectron spectroscopy (XPS) and low-energy ion scattering spectroscopy (LEIS). The selectivity conferred by two different SMIs, ethylbutyric acid, and pivalic acid has been compared experimentally and theoretically. Density Functional Theory (DFT) calculations reveal that selective surface functionalization using both SMIs is predominantly controlled thermodynamically, while the better selectivity achieved when using trimethylacetic acid can be explained by its higher packing density compared to ethylbutyric acid. By employing the trimethylacetic acid as SMI on other starting surfaces (Ta₂O₅, ZrO₂, etc.) and probing the selectivity, a broader use of carboxylic acid inhibitors for different substrates is demonstrated. It is believed that the current results highlight the subtleties in SMI properties such as size, geometry, and packing, as well as interleaved back-etch steps, which are key in developing ever more effective strategies for highly selective deposition processes.

B. Karasulu
Department of Chemistry
University of Warwick
Gibbet Hill Road, Coventry CV4 7AL, UK
E-mail: bora.karasulu@warwick.ac.uk
F. Roozeboom
Faculty of Science and Technology
University of Twente
HENGELOSESTRAAT, Enschede 7500 AE, The Netherlands
E-mail: f.roozeboom@utwente.nl
A. Mameli
TNO-Holst Centre
High Tech Campus 31, Eindhoven 6565 AE, The Netherlands
E-mail: alfredo.mameli@tno.nl

The ORCID identification number(s) for the author(s) of this article can be found under https://doi.org/10.1002/adma.202301204

1. Introduction

The ability to deposit patterned materials at precise locations is of paramount importance for technological advancement in catalysis,[1,2] energy harvesting,[3,4] and semiconductor device fabrication,[5] including metal oxide-based thin-film transistors.[6] In this respect, area-selective deposition (ASD) has attracted renewed interest,[7–16] particularly from the semiconductor industry, as a way to complement conventional *top-down* fabrication with more cost-effective *bottom-up* and *self-aligned* processes. ASD approaches relying on atomic layer deposition (ALD), for example, have also been explored for less challenging pattern sizes used in thin-film-transistors fabrication, which are typically employed in the display industry.[6] Generally in ASD, bottom-up structures are obtained by controlling heterogeneous surface reactions during deposition on a prepatterned substrate consisting of growth-areas (on which deposition is desired) and nongrowth areas (on which deposition is to be avoided). Such control is often exerted through selective manipulation of surface functional groups to either allow (on the growth area) or inhibit (on the nongrowth area) the deposition chemistry.[16,17]

ALD is a layer-by-layer deposition method that allows for atomic-level thickness control, conformality on 3D structures and large-area uniformity. In its most simple expression, ALD relies on the cyclic and alternating exposures of a substrate to a precursor and a coreactant that undergo self-limiting surface reactions.[18] ALD can offer optimal control over each individual surface reaction at the atomic level, during the precursor or the co-reactant step.[11,19,20] If sufficiently large differences in the thermodynamics and/or kinetics of the surface reactions exist on growth versus nongrowth areas, selective deposition can be naturally obtained, referred to as inherently selective ALD.[21,22] Often, however, the nongrowth area needs to be selectively modified so that thermodynamic or kinetic control over the ALD surface reactions can be achieved. Such modification can be performed either prior to the ALD process for example using self-assembled monolayers,[23] plasma or small molecule inhibitor (SMI) surface
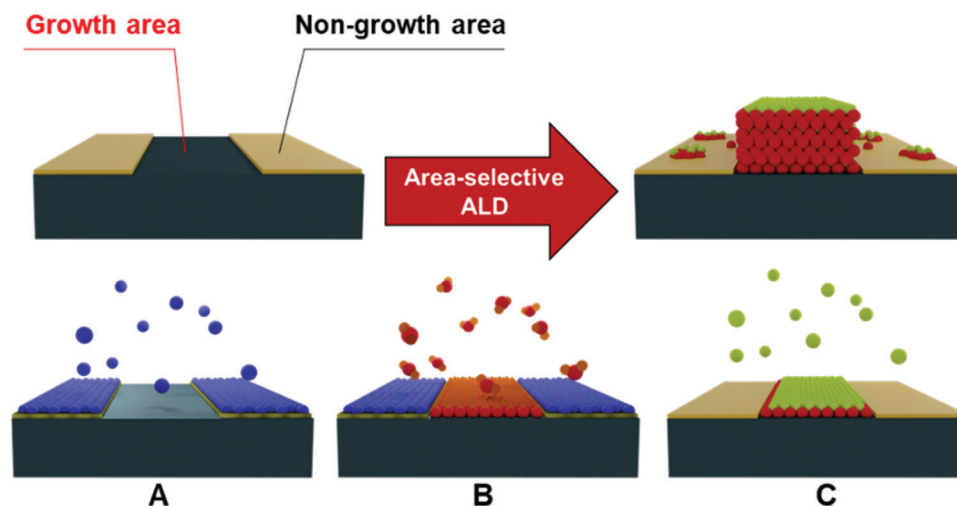
Figure 1. Schematic illustration of a generic area-selective ALD process consisting of three steps (A–C) in which the starting substrate is a patterned surface with two different materials: the growth area on which deposition is desired; and the non-growth area on which deposition ideally should not occur. In step A, a patterned substrate is exposed to a gas-phase SMI that selectively chemisorbs on the nongrowth area, thus de-activating it for further reaction with the precursor. In step B, the precursor surface reaction is inhibited on the de-activated non-growth area, hence selective precursor chemisorption takes place only on the growth area. In step C, the exposure to the coreactant produces the first sub-monolayer of selectively deposited material by surface reaction with the chemisorbed precursor. In addition, the coreactant can remove the inhibitor, especially in the case of plasma-activated coreactants. By repeating the ALD cycles, the intended material can be selectively deposited on the growth area. In reality, however, the selectivity is typically less than 100%, hence defects (e.g., unwanted deposition) occur on the non-growth area. Figure based on Ref. [26]

modifications,[24,25] or during the ALD process by inserting SMIs by coinjection or as a third separate step in the ALD recipe.[26,27]

Despite its great potential, the industrial exploitation of area-selective ALD (AS-ALD) to date is limited to only a few processes, and several technological challenges need to be overcome for wider acceptance. Amongst these, two major obstacles are high defectivity (i.e., the amount of unwanted material on the non-growth area) and low throughput. As illustrated in **Figure 1**, during AS-ALD a small amount of unwanted deposition is often observed on the nongrowth areas, failing the stringent selectivity requirements for many industrial applications, which call for 99.999% defect-free surfaces. Intermittent etching has been proposed as a possible solution for correcting and controlling the defectivity of an AS-ALD process or selective chemical vapor deposition (CVD) process.[9,28] Supercycles consisting of several AS-ALD cycles and etch correction steps can be repeated to obtain high selectivity and low defectivity, while increasing the thickness of the deposited layer through supercycle repetitions. Apart from the inherently low deposition rate, a major contribution for AS-ALD low throughput is the selective "passivation" of the nongrowth area, typically requiring several hours when applying self-assembled monolayers from liquid phase.[29] Recently, gas-phase SMIs (either as surface pretreatment, or coinjected with the precursor, or as integral part of the ALD cycle)[25–27] have been introduced as selective non-growth area passivating agents, significantly decreasing the time required for passivation and thus opening up more possibilities, including plasma-based AS-ALD processes.[26,30] This way, the passivation time is usually cut down to tens or hundreds of seconds (instead of minutes/hours).

As a proof-of-principle, here we present an approach that tackles both throughput and defectivity challenges by a unique combination of atmospheric pressure spatial-ALD supercycles interleaved with spatial etching steps that can be performed in the same processing tool, thus enabling AS-ALD with low defectivity and at a high throughput.

For the AS-spatial-ALD part we make use of the so-called *ABC-type* approach since it is an all-dry process and fully compatible with plasma-ALD chemistries, see also Figure 1.[26] Similar to the "ABC-type" AS-ALD approach utilizing acetylacetone as SMI,[26] this approach consists of three steps, as illustrated in Figure 1. By cycling the three steps, the thickness of the selectively deposited layer can be increased. In reality, however, the selectivity is typically degraded after tens of ALD cycles allowing for only a few nm-thick selective deposition. This is usually ascribed to the interplay of several surface properties and phenomena, such as surface defects, presence of various surface groups having different reactivity, coverage of the inhibitor layer, bulkiness of the precursor, surface modification during the coreactant step, etc. As a result, a nucleation delay is often observed on the non-growth area, before steady-state ALD growth kicks in as the number of cycles increases.

Two SMIs, namely ethylbutyric acid and trimethylacetic acid (also known as pivalic acid), were employed to develop ABC-type AS-ALD processes for SiO_2 film growth using an atmospheric pressure spatial ALD reactor (AS-spatial-ALD). Selective SiO_2 deposition of up to ≈8.0 and ≈3.5 nm thickness were demonstrated using these SMIs. At the same time, deposition rates ranging from 1 to 3 nm min^{-1} were achieved, resulting therefore in a substantial throughput increase. To put this into perspective, a GPC of 0.09 nm and a cycle time of ≈30 s have been employed for selective SiO_2 using Hacac, resulting in a deposition rate of ≈0.18 nm min^{-1}.[26] Hypothetically, a 5 nm thick SiO_2 layer would require 1.6 or 5.0 min (for 3 and 1 nm min^{-1} process, respectively) versus 27 min of processing time for conventional ALD.

A dedicated reactor design allowing for integrated film deposition and etch-back correction steps within the same deposition

ADVANCED
SCIENCE NEWS
www.advancedsciencenews.com

ADVANCED
MATERIALS
www.advmat.de

tool made it possible to further extend the selectively deposited SiO$_2$ thickness. No SiO$_2$ was detected on the ZnO nongrowth areas by both X-ray photoelectron spectroscopy (XPS) and low energy ion scattering (LEIS). By combining ABC-type AS-spatial-ALD with a newly developed spatial etching process in a supercycle fashion, we further extended the selectively deposited thickness from 3.5 up to 9 nm, using 3 supercycles, and up to ≈23 nm using pivalic acid as SMI and conventional plasma back-etching. When considering the combination with back-etching steps in conventional versus spatial, a cluster tool would be the method of choice for conventional (i.e., temporal) processes to avoid cross-contamination and process drifts, which complicates estimating differences in supercycle deposition rate for the two configurations. We, however, note that the spatial confinement and the reduced wall-to-surface ratio in a spatial configuration might be an additional benefit with respect to cross-contamination and process drifts.

Density functional theory (DFT) calculations were employed to unravel the underpinning chemistry for selective adsorption of the two SMIs on the nongrowth area, and their effect on the SiO$_2$ selectivity. DFT findings show that dissociative inhibitor binding is not energetically feasible on the SiO$_2$ surfaces. By contrast, the dissociative binding of both ethylbutyric acid and pivalic acid is thermodynamically and kinetically feasible on the ZnO nongrowth area.

DFT calculations further helped us in understanding some key features of SMIs that enable high selectivity. It was experimentally found that pivalic acid can almost double the selectivity (i.e., enabling longer nucleation delay on the nongrowth area). By simulating the binding of multiple molecules onto the ZnO surface using DFT, it was found that the better performance of pivalic acid as SMI compared to ethylbutyric acid can be ascribed to its higher packing density, which in turns allows for better precursor blocking.

We believe the unique advantages of this method not only allow for combining high-selectivity with low defectivity and high-throughput but will also enable new applications in roll-to-roll and very large area processing. Finally, we extend the AS-spatial-ALD process to other (non-)growth areas, and discuss generalized learning that can help in developing highly effective ASD processes.

2. Results and Discussion

2.1. ABC-Type Area-Selective Spatial ALD of SiO$_2$

2.1.1. Ethylbutyric Acid as Small Molecule Inhibitor

A series of SiO$_2$ ABC-type spatial ALD cycles was carried out on 150 mm c-Si wafers with coarse patterns (cm^2) of ZnO and c-Si (with native oxide) areas to investigate the impact of ethylbutyric acid as the SMI during the SiO$_2$ deposition on both starting surfaces. To this end, ethyl butyric acid, bisdiethylaminosilane (BDEAS) and O$_2$ plasma were continuously dosed from three separated slots of the spatial ALD injector head, corresponding to the steps A, B and C, as schematically illustrated in **Figure 2**a, see the Experimental Section for details. The substrate was rotated underneath the injector head at a speed of 20 RPM, corresponding to exposure times of 164 ms for each reactant (at a ra-

dial position of 35 mm). The patterned wafers were subjected to 20, 40, 80, and 150 ABC-type spatial ALD cycles, respectively. The resulting SiO$_2$ thickness was measured by ex situ spectroscopic ellipsometry (SE) on both ZnO and c-Si surfaces. Figure 2b shows the SiO$_2$ thickness evolution as a function of the number of ABC-type spatial ALD cycles on both ZnO and c-Si. A linear increase of thickness with the number of spatial-ALD cycles is observed for SiO$_2$ being deposited on c-Si, resulting in a growth per cycle (GPC) of ≈1.1 Å. This is slightly lower than the standard GPC of ≈1.4 Å, indicating that a small amount of inhibitor might still be adsorbing on SiO$_2$ and thus reducing the GPC. In strong contrast with what was observed for c-Si, a nucleation delay between 30 and 40 ALD cycles takes place on the ZnO surface. These results indicate preferential adsorption of ethylbutyric acid on ZnO and consequently, the effective inhibition of BDEAS chemisorption on the deactivated ZnO surface. The nucleation delay obtained with an ABC-type cycling on nongrowth ZnO surface means that a ≈3 nm SiO$_2$ film can be selectively deposited on c-Si substrate in the presence of ZnO.

Figure S1 (Supporting Information) shows the raw SE data as measured for different SiO$_2$ ABC-type spatial ALD cycles on the growth area, c-Si (Figure 4a) and on the nongrowth area, ZnO (Figure 4b). A rapid decrease in the phase shift, Δ, is observed on the c-Si surface, indicating thickening of the SiO$_2$ layer on this surface already after 20 cycles. In sharp contrast, negligible variations of Δ are observed after 20 cycles on the nongrowth area, thus validating the nucleation delay derived from optical modelling of SE data.

After 40 ABC-type AS-spatial-ALD cycles, an average SiO$_2$ thickness of 0.2 nm was measured by ex situ SE on the non-growth area, likely indicating the presence of SiO$_2$ islands on the ZnO nongrowth area.

Although such a nucleation delay already represents a major improvement with respect to the previously reported AS-ALD processes for plasma-based SiO$_2$,[26] it may still be insufficient for industrial applications. In particular, the resulting defectivity has to be extremely low (99.999% purity) to enable the industrial viability of such approach in advanced patterning and bottom-up fabrication strategies. In order to lower the defectivity and increase the selectively deposited film thickness, two main routes can be taken:

1) explore a more effective inhibition chemistry;
2) interleave etch-back steps to correct for selectivity loss.

Both strategies are explored and discussed below.

2.1.2. Pivalic Acid as SMI

Pivalic acid was investigated as a possible inhibitor with the reasoning that having a slightly different geometrical arrangement might afford a better precursor blocking. The surface coverage, bulkiness (steric hindrance) and geometrical arrangement of the chemisorbed inhibitor play a fundamental role in the degree of selectivity that can be obtained.[31] Considering this, we hypothesize that having a more "linear" arrangement the chemisorbed ethylbutyric acid can potentially leave more reactive sites accessible to the incoming precursor molecules. By contrast, a
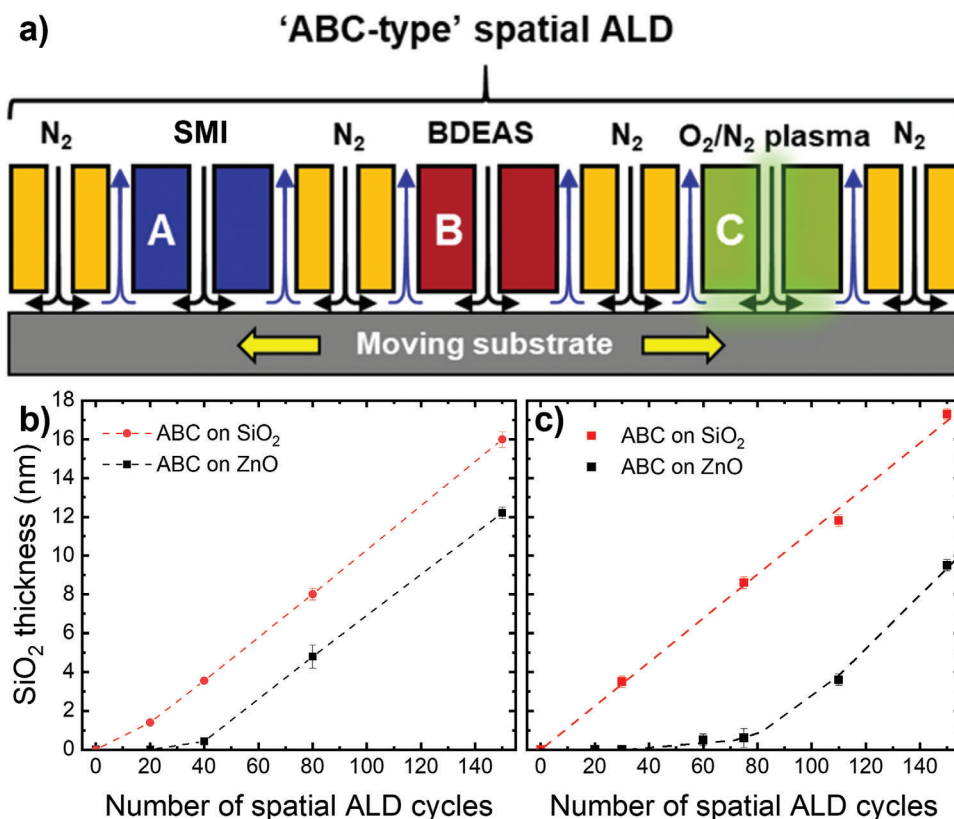
**ADVANCED
SCIENCE NEWS**

www.advancedsciencenews.com

**ADVANCED
MATERIALS**

www.advmat.de

Figure 2. a) Schematic representation of the spatial ALD injector head for the ABC-type area-selective spatial ALD used in this work. All reagents are continuously dosed from individual slots that are separated by inert N_2 gas curtains, while the substrate moves underneath the injector head. SMIs, ethylbutyric, or pivalic acid were used as the inhibitor (step A), bisdiethylaminosilane (BDEAS) as the silicon precursor (step B), and O_2 diluted in N_2 as the plasma coreactant (step C). Nucleation behavior for the ABC-type area-selective spatial ALD of SiO_2 on the growth area (c-Si with native oxide) and non-growth area (ZnO) using b) ethylbutyric acid and c) pivalic acid as SMI, as measured by ex situ spectroscopic ellipsometry. The dotted lines serve as a guide to the eye. Standard deviation is shown as error bar; 12 measurements at different locations over the same wafer were taken for each data point.

higher symmetry arrangement and a more compact size of the chemisorbed pivalic acid may offer a closer packing, thus effectively more steric hindrance, which translates into a better precursor blocking.

To test our hypothesis on the effectiveness of pivalic acid as an alternative inhibitor, another series of SiO_2 ABC-type spatial ALD cycles was carried out on 150 mm c-Si wafers with coarse patterns (order: cm^2) of ZnO and c-Si (with native oxide) areas. Thus, pivalic acid, BDEAS and O_2 plasma were continuously dosed from three separate slots of the spatial ALD gas injector head, corresponding to the steps A, B, and C of the ABC-type cycle. The substrate was moved underneath the injector head at a speed of 10 RPM, corresponding to exposure times to each reactant of 327 ms (radius = 35 mm). The patterned wafers were subjected to 30, 75, 110, and 150 ABC-type spatial ALD cycles, respectively. The resulting SiO_2 thicknesses were measured by ex-situ SE on both starting surfaces. Figure 2c shows the SiO_2 thickness evolution as a function of the number of ABC-type spatial ALD cycles on both ZnO and c-Si surfaces. Similarly to what was observed in the case of ethylbutyric acid, a linear thickness increase with the number of ALD cycles is observed for SiO_2 deposited on c-Si, resulting in a GPC of ≈ 0.11 nm. In contrast with what is observed for c-Si, a nucleation delay in the order of

$\approx 60–70$ ALD cycles takes place on the ZnO surface. These results point to a strong preferential adsorption of pivalic acid on ZnO and thus strong inhibition of BDEAS chemisorption. For this inhibitor, the nucleation delay translates into a ≈ 8 nm thick SiO_2 film that can be selectively deposited on c-Si in the presence of ZnO. This corresponds to a nucleation delay on ZnO that results in twice the SiO_2 thickness than what was obtained with ethylbutyric acid as the inhibitor, before the selectivity is severely degraded.

2.2. Surface Chemistry Behind Selective Inhibition

2.2.1. Energetics of Chemisorption on ZnO and SiO_2 Surfaces

In order to understand the chemical mechanism underpinning the selectivity achieved, we have performed a series of DFT calculations. Following from previous studies,[32] we employed a bare ZnO(10$\bar{1}$0) surface slab model, which is terminated by equal amounts of Zn and O surface sites (but no H), and it is considered to imitate a freshly cut/deposited ZnO substrate. However, it is possible that this ZnO surface might get hydrogenated/hydroxylated upon being exposed to air or background

Table 1. DFT reaction energetics for the pivalic acid and ethylbutyric acid inhibitor binding on a bare ZnO surface.

Binding orientation[a]	ΔE_p	ΔE_{TS}	ΔE_c – Prod1	ΔE_{TS}	ΔE_c – Prod2	ΔE_r	Remarks
Pivalic acid on bare ZnO surface							
Ori4	−0.65	0.39	−1.12	0.00	−2.17	−1.52	**Prod1**: monodentate product formation via H-transfer from pivalic acid to surface OH (including the rotation of H from outward to inward position); **Prod2**: mono to bidentate conversion
Ori9	−0.55	0.09	−1.18	0.00	−2.09	−1.54	**Prod1**: monodentate product formation via H-transfer; **Prod2**: mono to bidentate conversion
Ori11	−0.63	0.39	−1.64	0.12	−2.15	−1.52	**Prod1**: monodentate product formation via H-transfer (including the rotation of H from outward to inward), **Prod2**: mono to bidentate via rotation
Ori26	−0.57	0.00	−1.82	–	–	−1.25	**Prod1**: Barrierless, concerted H transfer and mono-bidentate product conversion
Ethylbutyric acid on bare ZnO surface							
Ori2	−0.43	0.33	−1.27	0.13	−1.63	−1.20	**Prod1**: monodentate product formation via H transfer (including the rotation of H from outward to inward), **Prod2**: mono to bidentate via rotation
Ori4	−0.55	0.00	−1.39	–	–	−0.84	Ethylbutyric acid-OH oxygen is already bonded to a surface Zn site; **Prod1**: Barrierless, concerted mono to bidentate conversion and H transfer
Ori5b	−0.60	0.14	−0.90	0.0	-1.20	−0.60	**Prod1**: monodentate product formation via H transfer (and rotation) **Prod2**: mono to bidentate conversion

[a] Energetics highly depend on the binding orientation of pivalic acid/ethylbutyric acid inhibitor molecules. Only some binding orientations (from the set of 26, Ori[1-26]) were selected for NEB calculations, as not all of them are in a reactive position. All corresponding minimum-energy paths (MEPs) are visualized in Figure S10a,b (Supporting Information).

moisture. To verify this notion, we have computed the average adsorption energies of H-atoms on a bare ZnO surface using models with varying surface H-coverage ratios (Table S1, Supporting Information). Resulting adsorption energies suggest that the hydrogenation of ZnO is thermodynamically not favorable (endothermic process). Along these lines, we have also checked the thermal stability of the different ZnO(10$\bar{1}$0) models using a temperature ramping procedure based on ab initio molecular dynamics (AIMD) (for details, see Computational Methodology in the Experimental Section). These AIMD simulations (their trajectories can be found in the Supporting Information) show that bare ZnO is stable up to high temperatures ($T \approx 1200$ K), whereas the hydrogenation of the surface leads to the abstraction of Zn atoms from the topmost layer. This leads to a surface reconstruction even at lower temperatures ($T \approx 600$ K). Taken together, the bare ZnO surface is predicted to be notably more stable than the H-terminated one. Therefore, in the inhibitor binding analysis following below, we only consider the bare ZnO surface model without any surface H-groups.

To understand how strongly the two inhibitors (ethylbutyric acid and pivalic acid) bind on the bare ZnO and SiO$_2$:H surfaces, we have performed a conformational analysis which covered multiple inhibitor binding positions, viz. Ori[1-26]. One can note that the physisorption strength for both inhibitors on either surface strongly depends on the binding orientation (Tables S2 and S3, Supporting Information). This is mainly due to the presence of two different chemical moieties in both inhibitors: the carboxyl and the alkyl groups, with the former interacting more strongly with the surface Si–OH and Zn–O groups via hydrogen bonds (Figures S2–S5, Supporting Information).

As also evident from the average binding energies (Table S2 and S3, Supporting Information), pivalic acid is predicted to typically physisorb more strongly than ethylbutyric acid on both bare ZnO and SiO$_2$:H surfaces (average $\Delta E_p = -0.26$ vs 0.09 eV for ZnO and $\Delta E_p = -0.63$ vs −0.29 eV for SiO$_2$ surface). This can be ascribed to the fact that ethylbutyric acid has more bulky side groups consisting of longer alkyl chains (creating larger steric hindrance) and more electropositive centers (Figures S2–S5, Supporting Information). In addition, both ethylbutyric acid and pivalic acid overall tend to physisorb more strongly on the SiO$_2$ surface than on the bare ZnO surface (average physisorption energy, $\Delta E_p = -0.63$ vs −0.26 eV for pivalic acid and $\Delta E_p = -0.29$ vs 0.09 eV for ethylbutyric acid, see Tables S2 and S3, Supporting Information). This can be ascribed to the higher ratio of oxygen sites per surface area on the SiO$_2$ surface than that of ZnO ($\approx$10 oxygen per nm^2 vs 6 oxygen per nm^2), which facilitates stronger hydrogen bonding interactions, i.e., stronger physisorption, between the SiO$_2$ surface and inhibitors.

Even though strong physisorption is an important factor for an inhibitor sticking on a surface, without a strong chemisorption (dissociative binding), physisorbed adsorbates can be easily removed from the surface in a subsequent gas purging cycle. Therefore, we next inspected the chemisorption strength of ethylbutyric acid and pivalic acid on both surfaces by calculating the reaction energies of dissociative binding products using DFT (**Tables 1** and **2**). Notably, despite our efforts, we could not identify any energetically favorable mechanisms for the dissociative binding of both ethylbutyric acid and pivalic acid on SiO$_2$. In our numerous trials, whereby we simulated various chemisorbed products as input structures, geometry optimizations mainly converged

**ADVANCED
SCIENCE NEWS**

www.advancedsciencenews.com

**ADVANCED
MATERIALS**

www.advmat.de

Table 2. Reaction energetics for the pivalic acid and ethylbutyric acid inhibitor binding on an SiO_2:H surface.

Binding orientation[a]	ΔE_p	ΔE_{TS}	ΔE_c	ΔE_r	Remarks
Pivalic acid on SiO_2:H surface					
Prod A	−0.84	2.53	0.39	1.23	$SiO\text{-}CO(CH_3)_3{}^*$ +H_2O (g) (—OH from pivalic acid)
Prod B	−0.66	1.78	0.09	0.75	$SiO\text{-}C\text{-}(CH_3)_3{}^*$ + CHOOH (g)
Ethylbutyric acid on SiO_2:H surface					
Prod A	−0.63	1.08	0.03	0.66	$SiO\text{-}COH(CH_2\text{-}CH_3)_2{}^*$ + H_2O (g) (—OH from ethylbutyric acid)
Prod B	−0.38	4.15	0.92	1.30	$SiO\text{-}CH(CH_2\text{-}CH_3)_2{}^*$ + CHOOH (g)
Prod C	−0.58	0.68	-0.17	0.41	$SiO\text{-}COOH^*$ + $(CH_2)_3(CH_3)_2$; proceeding through the release of a CO_2 molecule

[a] All corresponding minimum-energy paths (MEPs) are visualized in Figure S10c (Supporting Information).

to the desorbed products that are energetically more favorable, whereas the chemisorbed species were formed through highly endothermic paths (ΔE_r = 0.41–1.23 eV) (see Figures S6 and S7 in the Supporting Information for some examples). Similarly, the binding of both inhibitors on SiO_2 is kinetically hindered, being associated with high activation energies (see Table 2).

Because SiO_2 has different hydroxyl surface groups (e.g., isolated vs H-bonded)[33] which can show distinct reactivities toward ALD precursors/inhibitors, the effect of hydroxyl coverage over the adsorption of SMIs was also checked. Relatedly, the removal of increasing amounts of hydrogen atoms from the SiO_2 surface is predicted to enhance the physisorption strength of ethylbutyric acid on the surface (Figure S8, Supporting Information). This might explain the lower GPC observed in the ABC-type SiO_2 ALD process.

Chemisorption of both pivalic acid and ethylbutyric acid, by contrast, is energetically feasible on bare ZnO, as is visible from the highly exothermic processes accompanied by small to none activation energies (Table 1). AIMD simulations at different temperatures reveal that the chemisorption of both inhibitors on the ZnO surface involves an H-atom transfer from the OH group of the inhibitor to the nearby surface oxygen site (see the Supporting Information for AIMD movies). In addition, one or both oxygen atoms from the inhibitor's carboxyl group will bind on one or two (neighboring) Zn sites on the surface, forming monodentate versus bidentate products, respectively (**Figure 3**). Geometry optimizations suggest that the bidentate products for both ethylbutyric acid and pivalic acid tend to yield more stable binding than the monodentate form (with an energy difference of 0.3–1.3 eV per adsorbate, Figure S9, Supporting Information). The conversion of a monodentate product to bidentate (usually via the rotation of the inhibitor's alkyl group) is predicted to be a barrierless exothermic process (Table 1 and Figure S10, Supporting Information).

In addition, the tandem processes (i.e., H-transfer from the inhibitor's carboxyl group and binding of the carbonyl groups to Zn site(s)) can occur concertedly or in varying order, as predicted by the static DFT calculations and AIMD simulations. The reaction path taken primarily depends on the binding orientation of the inhibitor on a given surface. Unlike the H-transfer and monodentate-bidentate conversion processes that proceed without an energy barrier, rotation/flip of a hydroxyl group – needed to align the –OH group for a subsequent H-transfer – involves
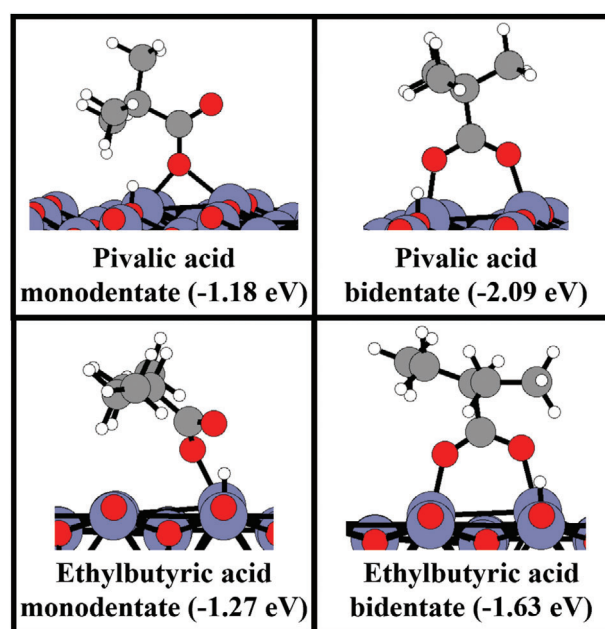

Figure 3. Comparison of the monodentate (left) and bidentate (right) product forms for (top) pivalic acid and (bottom) ethylbutyric acid inhibitors binding on a bare ZnO surface in selected binding orientations. An extended collection of mono/bidentate products identified for different binding orientations is given in Figure S9 in the Supporting Information.

a minor energy barrier (ΔE_{TS} = 0.13–0.39 eV, Table 1). The latter is likely the rate-limiting step in the binding of ethylbutyric acid and pivalic acid on a bare ZnO surface, which are otherwise barrierless processes.

Comparing the DFT energetics for the chemisorption of pivalic acid and ethylbutyric acid inhibitors on bare ZnO surface, we note that the pivalic acid is predicted to bind stronger than ethylbutyric acid in view of overall more exothermic reaction energies (ΔE_r = −1.3 to −1.6 eV for pivalic acid versus ΔE_r = −0.5 to −1.2 eV for ethylbutyric acid, see Table 1). As for its stronger physisorption, the stronger chemisorption of pivalic acid compared to that of ethylbutyric acid can be ascribed to its less bulky alkyl side groups, reducing the steric hindrance. In contrast, in terms of kinetics no clear distinction is predicted for both inhibitors, i.e., for both SMIs the chemisorption processes occur without an
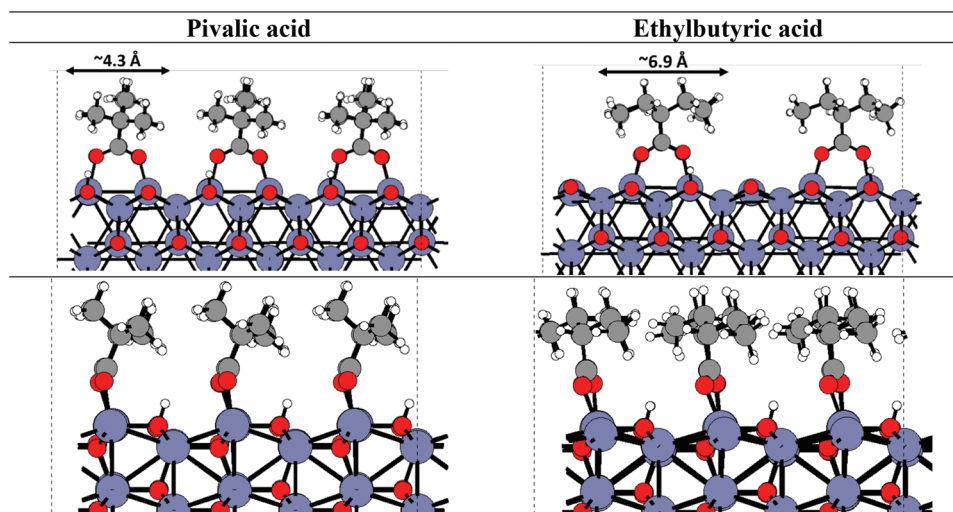
**ADVANCED
SCIENCE NEWS**

www.advancedsciencenews.com

**ADVANCED
MATERIALS**

www.advmat.de

Figure 4. Multiple inhibitor binding and surface coverage analysis: optimized structures of pivalic acid and ethylbutyric acid molecules chemisorbed on the surface via the most likely mechanism as predicted by DFT, visualized at two viewing angles (both side views). The alkyl group span is 4.3 Å for pivalic acid and 6.9 Å for ethylbutyric acid. The surface area of the model used here is 296.9 Å^2, which can accommodate 9 pivalic acid and 6 ethylbutyric acid molecules. Spacings between two adjacent ethylbutyric acid molecules (multiple surface oxygen sites remain available) are noted, whereas pivalic acid is predicted to block all oxygen sites.

energy barrier. This suggests that the selectivity is controlled by thermodynamics rather than kinetics.

Even in the case of a prehydrogenated ZnO surface (ZnO-H), DFT energetics suggest that the binding of both ethylbutyric acid and pivalic acid is both thermodynamically and kinetically feasible—even though they are likely to proceed via a different mechanism on ZnO:H, e.g., volatile H$_2$O byproduct release rather than a H-atom transfer (Table S4, Supporting Information).

Taken together, these DFT findings support the notion that the dissociative inhibitor binding is not energetically feasible on the SiO$_2$:H surface, even though SiO$_2$ as a substrate facilitates a stronger physisorption for both ethylbutyric acid/pivalic acid inhibitors than ZnO does. By contrast, the dissociative binding of both ethylbutyric acid and pivalic acid is energetically (both thermodynamically and kinetically) highly feasible on the ZnO surface, enabling an efficient and homogeneous inhibitor binding on the surface.

2.2.2. Surface Coverage and Packing Considerations

Besides the sticking probability of the inhibitor, another factor controlling the selectivity is the effective blockage of the available surface adsorption sites against the subsequent ALD precursor binding. Along these lines, we have checked the surface coverage provided by the two inhibitors by simulating several inhibitors simultaneously chemisorbed onto the bare ZnO surface, while considering the likely binding mechanism as identified above, i.e., H-atom transfer from inhibitor to the surface oxygen site and bidentate product, see **Figure 4**. Having a larger side-chain span (ethylbutyric acid: 6.9 Å vs pivalic acid: 4.3 Å), more spacing is required between two neighboring ethylbutyric acid molecules than those of pivalic acid. As a result, more pivalic acid molecules can stick per surface area (9 pivalic acid vs

Table 3. Chemisorption energies (eV molecule^{-1}) for multiple ethylbutyric acid/pivalic acid inhibitor binding on a bare ZnO(10$\bar{1}$0) surface.

Number of inhibitors	ΔE_c/pivalic acid	ΔE_c/ethylbutyric acid
1	−2.20	−1.66
2	−2.20	−1.65
3	−2.23	−1.65
4	−2.25	−1.66
6	−2.23	−1.70
9	−2.29	—a)

a) A maximum of six ethylbutyric acid inhibitors could be fitted into the current ZnO surface model (area of 296.9 Å^2), while adding more ethylbutyric acid led to unstable structures due to high steric hindrance (electrostatic interactions).

6 ethylbutyric acid molecules within ca. 3 nm^2). In principle, all oxygen sites can be blocked by pivalic acid (assuming a regular sticking/close-packing pattern is achieved), while at least three rows of Zn/O sites remain available between two adjacent ethylbutyric acid molecules for a precursor binding at a subsequent cycle.

In addition, for both pivalic acid and ethylbutyric acid the chemisorption energy per inhibitor molecule remains fairly constant (maximum variation of only 0.09 eV when going from 1 to 9 pivalic acid molecules simultaneously bonded on ZnO and maximum variation of only 0.05 eV for 1–6 ethylbutyric acid molecules bonded on the surface), with more molecules binding simultaneously on the surface, indicating a sufficient spacing hence minimal interactions between the two closest pair of adsorbates (**Table 3**).

In other words, multiple inhibitor binding is predicted not to change the adsorption thermodynamics and also kinetics, given the barrierless binding processes. In line with the single-adsorbate results discussed above, multiple pivalic acid
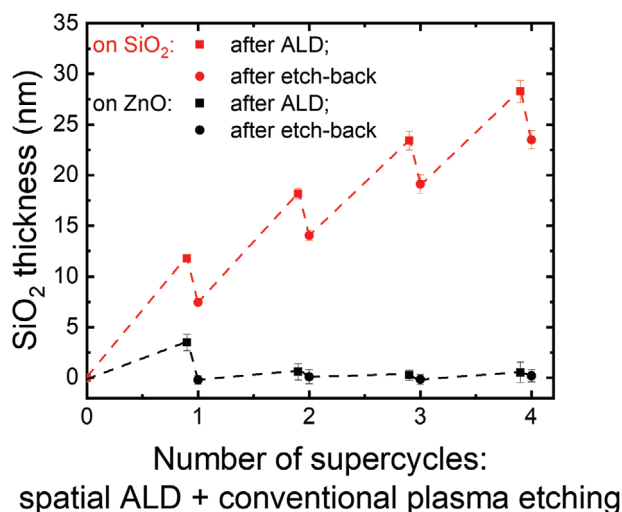
ADVANCED
SCIENCE NEWS

www.advancedsciencenews.com

ADVANCED
MATERIALS

www.advmat.de

Figure 5. SiO_2 thickness as measured by ex situ spectroscopic ellipsometry: after 110 AS-spatial-ALD cycles on ZnO (■) and on SiO_2 (■), and after 3 s CF_4 plasma back-etching correction step (●) on ZnO and (●) on SiO_2. A supercycle is composed of 110 ALD cycles followed by a 3 s CF_4 etch-back step . In total four supercycles were performed using pivalic acid as SMI, allowing to reach a thickness of 23.5 nm SiO_2 selectively deposited on c-Si with native SiO_2, while no SiO_2 was measured on the ZnO nongrowth area. Standard deviations are shown as error bar; 4 measurements at different locations over the same wafer were taken for each data point.

molecules can bind on the ZnO surface more strongly than ethylbutyric acid at any surface coverage ratios (on average $\Delta E_c =$ −2.88 eV vs −2.54 eV per adsorbate). Taken together, DFT simulations suggest that by being able to fit and stick in a more close-packing pattern on the ZnO surface, pivalic acid can provide a more efficient blocking of the surface against a subsequent precursor adsorption, and thereby provide a better surface selectivity than ethylbutyric acid. In addition, amongst the three SMIs, pivalic acid has the highest binding energy on ZnO, which suggests that its eventual displacement by the BDEAS precursor is less likely.[34] These results point toward two important and characteristic criteria for the effectiveness of SMIs: relatively high coverage and high stability, i.e., strong bonding with the nongrowth area.

2.3. Interleaving Back-Etching Correction Steps

2.3.1. Proof-of-Principle with Conventional Plasma Etching

In order to further improve the selectivity, the process employing pivalic acid as the SMI was interleaved with conventional CF_4 plasma back-etching steps using a separate low-pressure plasma etching tool, as described in the Experimental Section. Following from the etch rate tests ($\approx$1.3 nm s^{-1}), an etch-back correction step of 3 s was employed to correct for the selectivity loss after 110 ABC-type spatial-ALD cycles. The number of cycles was optimized to facilitate the tracking of the SiO_2 thickness by SE after each half-supercycle, i.e., after each 110 ALD cycles and after each 3 s of CF_4 plasma etching.

Figure 5 shows the SiO_2 thickness on c-Si and ZnO surfaces after each 110 spatial ALD cycles using pivalic acid as SMI and after

3 seconds of plasma etching. A total of 4 supercycles resulted in $\approx$23.5 nm selective deposition of SiO_2 on c-Si versus ZnO, thus highlighting the benefit of such a powerful "dep-etch" combinatorial strategy. We note, however, that the first supercycle differs from the subsequent three on both growth and non-growth areas. In particular, a lower growth rate is observed after the first etch-back correction step on both surfaces. The calculated GPC values of SiO_2 on the growth area are $\approx$0.11 nm in the first supercycle, $\approx$0.10 nm in the second supercycle, and $\approx$0.08 nm in the subsequent two supercycles. On the nongrowth area 3.5 nm of SiO_2 is deposited in the first supercycle, 0.6 nm, 0.3 nm and 0.5 nm in the subsequent three supercycles. Thus a 10–25% decreased growth is observed on the growth-area and up to 86% on the non-growth area following the first supercycle which points toward additional inhibition effects of fluorocarbon residues generated during the plasma etching step.

In order to unravel the reasons behind this behavior, LEIS measurements were taken on the ZnO surface to quantify the selectivity of the first supercycle down to the sub-monolayer level and observe chemical changes upon back-etching. In particular the surface coverage and the thickness of SiO_2 deposited on the ZnO nongrowth area were monitored after 20, 60, and 110 cycles and after the 3 s of plasma etching. To this end, individual patterned samples were prepared with different numbers of cycles (without subsequent back-etching) plus one sample with 110 ABC-type spatial ALD cycles followed by 3 s of plasma etching.

Figure 6 shows the SiO_2 surface coverage and thickness on the ZnO surface. After 20 ABC-type spatial ALD cycles no SiO_2 on ZnO could be detected by LEIS, which further demonstrates the excellent selectivity of the process employing pivalic acid as SMI. As expected, the selectivity degraded with increasing number of cycles. After 60 cycles, a SiO_2 surface coverage of $\approx$68% was measured indicating Volmer–Weber island-type SiO_2 growth on the ZnO surface. The SiO_2 LEIS signal was calculated to correspond to a thickness of 2.2 nm. This is in contrast with the thickness measured by SE ($\approx$0.5 nm). Such discrepancy can be explained with the basic principle of SE measuring an average thickness over the entire probing area coupled to the optical modelling assuming a fully closed layer. On the contrary, LEIS measures the averaged thickness of the SiO_2 islands only. After 110 cycles, a SiO_2 surface coverage of 85% was measured by LEIS, corresponding to a film thickness of $\approx$3.4 nm, which this time is more in line with the SE measured thickness, i.e., 3.6 nm, as the SiO_2 layer now approaches a fully closed layer. After 3 s of plasma etching, no SiO_2 was detected by LEIS, indicating the complete recovery of the initial ZnO nongrowth area.

At this point, only 3 at% fluorine was detected by LEIS on the surface. This can be ascribed to the atomic oxygen cleaning step prior to the LEIS analysis, as described in the Experimental Section. A larger amount of fluorine and potentially CF_x species might be present on the ZnO surfaces after the plasma etch correction step. Such surface contamination could be responsible for the differences in thickness observed in the subsequent supercycles and may be accumulating on both surfaces with the increasing number of supercycles.

To test this notion, XPS measurements were taken on both ZnO and SiO_2 surfaces after 4 supercycles, see Figure S11 in the Supporting Information. Besides confirming the absence of SiO_2 on the ZnO surface (Si detection limit 0.3 at%) and hence, the
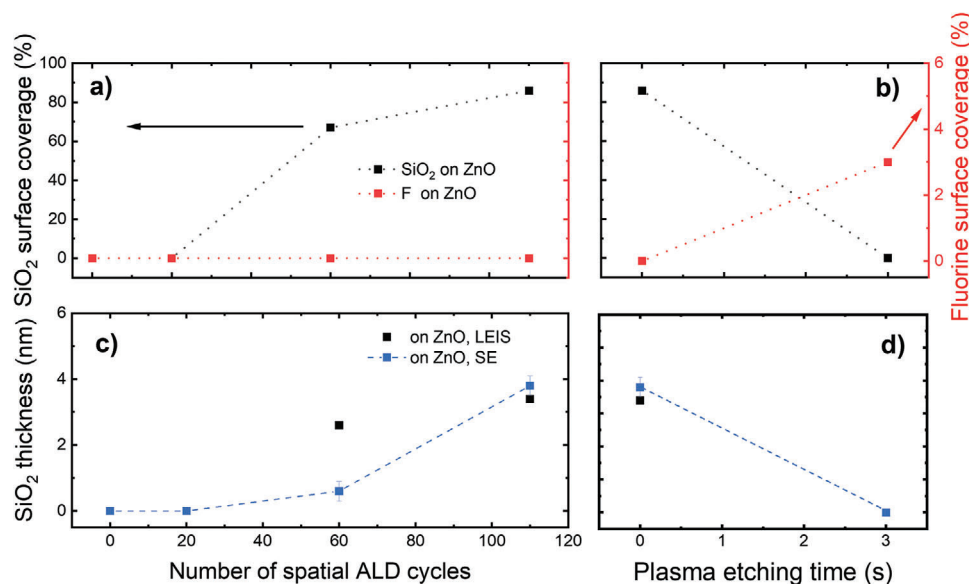
**ADVANCED
SCIENCE NEWS**

www.advancedsciencenews.com

**ADVANCED
MATERIALS**

www.advmat.de

Figure 6. SiO$_2$ surface coverage (■) and F surface coverage (■) on the ZnO non-growth area as measured by LEIS, as a function of a) the number of spatial ALD cycles, b) before and after 3 s of CF$_4$ plasma etching. SiO$_2$ thickness measured both by SE (■) and LEIS (■) as a function of c) the number of spatial ALD cycles, d) before and after 3 s of CF$_4$ plasma etching. Standard deviation is shown as error bar; 12 measurements at different locations over the same wafer were taken for each data point.

high selectivity of the combined "deposition-etch" approach, an intense peak related to fluorine was detected on ZnO surfaces and to a smaller extent also on SiO$_2$ surfaces. The amounts of fluorine present on the ZnO and SiO$_2$ surfaces after the etch-back step, 13 and 1 at%, respectively, can explain the differences in growth rates for different numbers of supercycles. Measures to counteract this effect should be therefore taken in order to ensure better process control. To this end, an additional O$_2$ plasma cleaning step was added after the back-etching step for the following experiments.

2.3.2. Spatial Plasma Etching of SiO$_2$

The supercycling approach using a separate tool for conventional plasma etching provides a proof of feasibility for achieving extremely high selectivity and good insights into the role of the etch-back correction step in supercycle reproducibility. Exchanging the wafer from a spatial ALD tool to a conventional plasma etcher, however, defies the purpose of the spatial approach, which is about maximizing throughput. To address this issue a novel dedicated atmospheric-pressure spatial plasma etching process was developed, to be able to run a complete supercycle on an integrated tool platform.

The same dielectric barrier discharge (DBD) plasma source, which was employed for the ABC-type AS-spatial-ALD process, was used to generate F-radicals and etch thermally grown SiO$_2$, as illustrated in **Figure 7**a. For these experiments, only CF$_4$, O$_2$, and N$_2$ gases were dosed through the plasma slot with (dynamic mode) and without (static mode) substrate motion. Figure 7b shows the normalized SiO$_2$ etch rate as a function of the O$_2$ ratio with respect to the total amount of O$_2$ and CF$_4$ flows in sccm. Both CF$_4$ and O$_2$ flows were diluted in N$_2$ to a total flow of 10 slm

to ensure cooling of the DBD plasma source. All the experiments plotted in Figure 7b were performed in the static mode, i.e., without rotating the sample underneath the injector head, and with a total etching time of 1 min. for each data point.

The DBD plasma source was operated at 65 kHz and a supplied voltage of 120 V. Similar to what was observed in conventional low-pressure plasma etching, the SiO$_2$ etch rate initially increased with increasing O$_2$ percentages, reached a maximum and then decreased to zero when no CF$_4$ was fed to the plasma source. The maximum etch rate occurred at 12.5% O$_2$, calculated as ratio of flows sccm (O$_2$)/[(sccm(O$_2$) + sccm(CF$_4$)], which is about half of the values observed for low-pressure conventional etching.[35,36] The appearance of a maximum in the etch rate as a function of the O$_2$ content in the CF$_4$-O$_2$ mixture is a well-known effect, and it is due to the initial increase in fluorine concentration, which is the active etchant species. Further increasing the O$_2$ content will dilute the concentration of fluorine-containing species. However, the reasons for the different peak position are not yet known at present and beyond the scope of this work.

For the dynamic (i.e., rotating the wafer underneath the plasma source) etching experiments, the plasma settings were fixed at 120 V, 12.5% O$_2$ and 65 kHz. A total of 100 rotations was performed at different rotation speeds: 30, 10, 5 RPM and the etch rate was calculated by the measured thickness differences (before and after etching) divided by the total exposure time underneath the plasma. Figure 7c shows the measured etched thicknesses as a function of the total exposure time. Linear fitting resulted in an etch rate of 0.32 ± 0.01 nm s^{-1}.

The effect of the substrate temperature on the etch rate was also investigated up to 200 °C, see Figure S12 in the Supporting Information for more details. Using the Arrhenius plot (etch rate vs 1/T) an apparent activation energy of 0.23 ± 0.02 eV was obtained. This is in agreement with the values reported in the
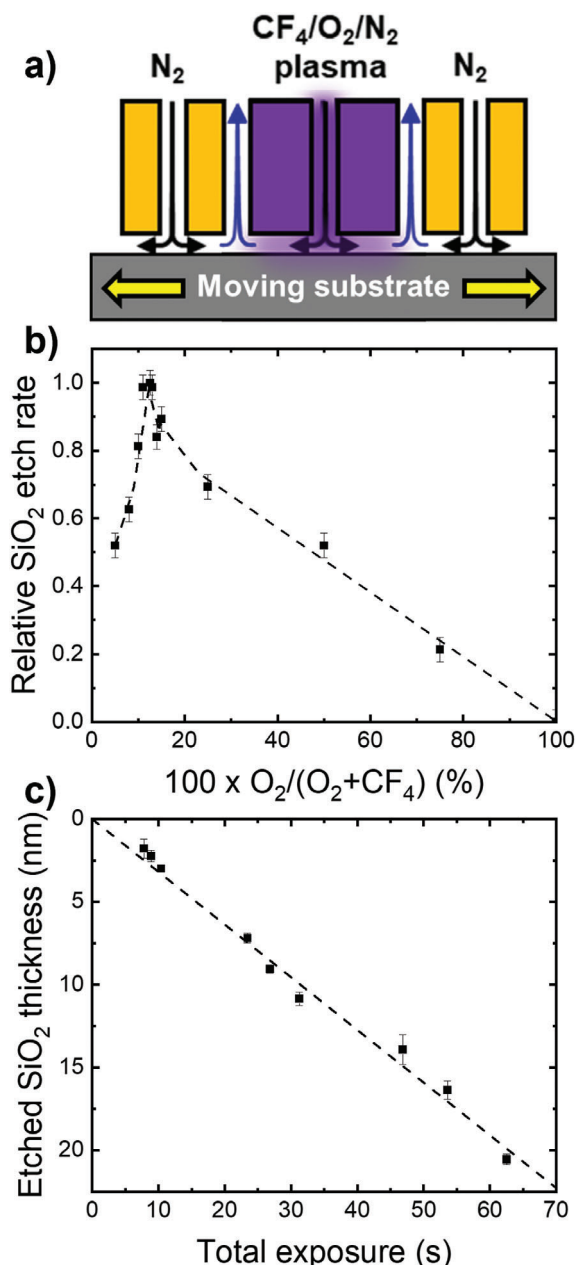
2.3.3. Integrated Approach for ABC-Type Spatial ALD with Spatial Plasma Etching in Supercycle Fashion

In order to develop a fully integrated spatial plasma deposition-etch process, supercycle recipes were tested with the same plasma source being used both for depositing and etching. Hence, a short interval between deposition and etching steps was necessary to allow for switching between different gases and settings. In this case, we opted for the ethylbutiric acid SMI to demonstrate the robustness of the combined approach. As depicted in **Figure 8**a, a supercycle approach was developed which consisted of $m = 40$ ABC-type AS-spatial-ALD cycles, using ethylbutyric acid as SMI, and $n = 6$ spatial $CF_4/O_2/N_2$ plasma etching correction "cycles." In total three supercycles were performed. The 6 etching "cycles" were carried out at 20 RPM (same rotational speed as the ABC-type AS-spatial-ALD process) to ensure that all unwanted SiO_2 was removed from the non-growth area. Based on the etch rate calculated from Figure 7c, a total SiO_2 etched thickness of around 0.3 nm for an exposure time of 160 ms should be expected. The SiO_2 thickness on both surfaces was measured after every half-supercycle, i.e., after 40 ALD cycles and after 6 etching "cycles" that together composed one supercycle.

Figure 8b shows the SiO_2 film thickness as measured by ex situ SE. After the first 40 ABC-type spatial ALD cycles (using ethylbutyric acid as SMI), SiO_2 thicknesses of ≈3.6 nm and ≈0.4 nm were measured on c-Si and ZnO, respectively, indicating that only a minor deposit of SiO_2 is present on the latter (nongrowth area). The subsequent 6 cycles of $CF_4/O_2/N_2$ plasma etching resulted in a SiO_2 thickness decrease of ≈0.3 nm on the growth area, while the SiO_2 was completely removed from the ZnO surface. To counteract the effect of fluorine contaminations on both surfaces, an O_2 plasma cleaning step (20 rotations at 20 RPM) was inserted in between supercycles, as described in Section 2.3.1. Figure 8b also shows that after three supercycles a SiO_2 thickness of 9.6 nm was measured on the growth area, while no SiO_2 formation was detected on the non-growth area. This demonstrates the high selectivity of the integrated approach using spatial ALD and etching within the same tool. In addition, we note that residuals of the SMIs may be incorporated in the SiO_2 layer, which depending on the application can even be advantageous since carbon incorporation would lower the dielectric constant of SiO_2. Similarly to what has been observed with fluorine contaminations, fine-tuning of the O_2 plasma step and/or the deposition temperature can remove most, if not all, carbon.

Figure S13 (Supporting Information) shows the raw SE data for each half-supercycle. In agreement with our ellipsometry measurement (Figure S1, Supporting Information), a decrease in Δ on the c-Si surface is observed after the first 40 cycles. This is followed by a slight increase after the etching half-supercycle step, consistently with decreased SiO_2 thickness due to etching. The same trend is observed for the subsequent two supercycles and the net result corresponds to a larger SiO_2 thickness than the starting point. On the ZnO nongrowth area, a small decrease in Δ is observed, which corresponds to minor deposition on the ZnO surface. Upon etching, Δ is back to the starting situation, which indicates that the unwanted SiO_2 deposition is removed from the nongrowth area. After three supercycles it is difficult to distinguish the processed ZnO surface from its initial status,
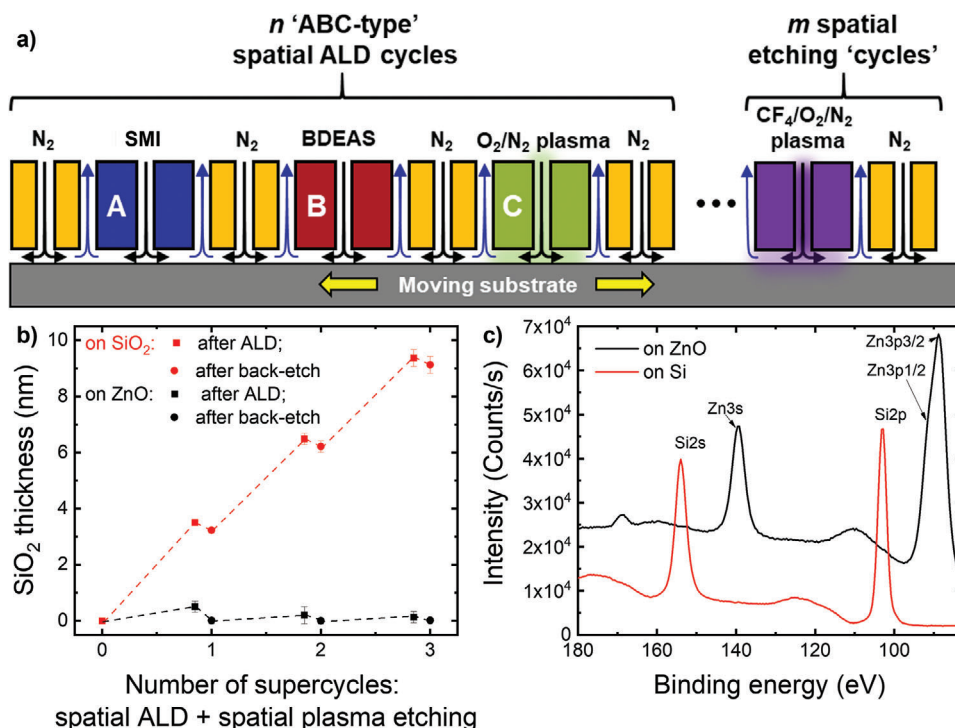

Figure 7. a) Schematic representation of the plasma etch gas injector head used in the rotary spatial ALD reactor. b) Normalized SiO_2 etch rate as a function of the O_2 percentage with respect to CF_4 (further diluted in N_2 to 1000 sccm). The dashed lines serve as a guide to the eye. Ellipsometry fitting error before and after etching was propagated to derive the error bars. c) Etched SiO_2 thickness after 100 etching "cycles" as a function of the total exposure time. Standard deviations are shown as error bar; 3 measurements at different locations over the same wafer were taken for each data point.

literature for low-pressure etching,[37] suggesting that the underlying etching mechanism is the same in both etching processes.[37,38] See also Table S5 (Supporting Information) for a short overview of the etch rates for different plasma sources and pressures.

**ADVANCED
SCIENCE NEWS**

www.advancedsciencenews.com

**ADVANCED
MATERIALS**

www.advmat.de

Figure 8. a) Concept for an integrated injector head combining both "ABC-type" ALD and plasma back-etching in a supercycle-based spatial atmospheric-pressure mode to obtain high selectivity, high throughput, and low defectivity. b) SiO_2 film thickness as measured by *ex-situ* spectroscopic ellipsometry after 40 AS-spatial-ALD cycles on ZnO (■) and on SiO_2 (■), followed by 6 "cycles" of etching correction step (●) on ZnO and (●) on SiO_2, together constituting a supercycle. In total three such supercycles were carried out, allowing to reach a thickness of ≈9 nm SiO_2 selectively deposited on c-Si, while no SiO_2 was measured on the ZnO non-growth area. Standard deviations are shown as error bar; each sample was measured at 7 different locations of the wafer. c) XPS surface spectra of the growth areas (c-Si, red) and non-growth areas (ZnO, black) after three supercycles. No Si-related signal was detected on the nongrowth area, demonstrating the extreme selectivity of the spatial supercycle approach.

pointing toward high selectivity, see also Figure S14 (Supporting Information).

XPS line scans were performed on the ZnO pattern and on the c-Si pattern, to verify the selectivity measured by SE. Figure 8c shows the results at one point of the XPS line scans, here no silicon signal could be detected on the ZnO surface, demonstrating the high selectivity of the approach. The complete set of XPS line scans can be found in Table S6 (Supporting Information). On the growth area (c-Si) instead, the absence of a Si elemental peak at a binding energy of 99 eV confirms deposition of relatively thick SiO_2 since an average penetration depth of about 7 nm is expected for the employed XPS system, and a thickness of 9.1 nm SiO_2 was selectively grown on top of the native (1.7 nm) SiO_2.

The last process step was a $CF_4/O_2/N_2$ plasma etch, i.e., no final O_2 plasma cleaning was performed, thus 13% and 1% F were found, respectively, on the nongrowth and growth area. The fluorine content and binding energy is attributable to the formation of ZnF_2 and some CF_x contamination left on the surface. A small percentage of fluorine on the deposited SiO_2 film is likely due to an incomplete etching reaction.

2.3.4. Extension to Selective-Area SiO_2 Deposition with Other (Non-)Growth Materials

In order to extend the newly developed process to more growth and nongrowth area materials, a few different materials were

tested using the ABC-type area-selective ALD approach employing the pivalic acid as inhibitor. A total of 60 ALD cycles was performed and the resulting SiO_2 thickness was measured by LEIS, with the exception of SiO_2 deposition on SiO_2 substrate which was estimated by the GPC of the ABC-type process. As can be seen in **Table 4**, different degrees of inhibition were observed depending on the starting surface. This points toward different reactivity and/or packing density of the pivalic acid on different surfaces, and also reveals a more generic use of carboxylic acid inhibitors beyond the ZnO and SiO_2 surfaces used as study cases. The different extent of pivalic acid chemisorption on different surfaces (and thus the differing SiO_2 thicknesses following from a nucleation delay) can be rationalized in terms of acid/basic character of the oxide surface. Here, we use a previously reported criterion, relating the extent of NH_3 and CO_2 adsorption on diverse metal oxide surfaces to their covalent versus ionic character.[39] Despite its simplicity, this method provides a very intuitive way to gauge the relative amount of acidic/basic sites for different oxides: a higher ionic character relates to a more basic character, whereas a higher covalent character leading to higher acidity. In addition, the surface acidity scale based on the Sanderson's electronegativity method is also reported in Table 4.[40] Except for TiO_2, a relatively good agreement between acidity and extent of nucleation delay (i.e., measured thickness after 60 ALD cycles) is found for all surfaces, especially when using the charge/cation's ionic radius acidity scale. For the case of MoCr and IGZO we could not calculate the charge/ionic radius ratio since the

**ADVANCED
SCIENCE NEWS**

www.advancedsciencenews.com

**ADVANCED
MATERIALS**

www.advmat.de

Table 4. SiO_2 thickness and surface coverage as measured by LEIS for different starting surfaces, together with the charge/cation radius ratio and the acidity scale based on Sanderson's electronegativity as estimates of surface acidity[a].

Starting surface[a]	SiO_2 thickness [nm]	SiO_2 coverage [%]	Charge/cation radius [b]	Sanderson's acidity scale [c]
SiO_2	6.6 ± 0.3		10.0	2.73
MoCr	4.4	99	n.a.	n.a.
Ta_2O_5	3.5	100	6.8	2.28
ZrO_2	3.4	n.a.	5.0	1.07
SnO_2	3.1	100	5.6	2.88
IGZO [d]	2.6	n.a.	n.a.	n.a.
ZnO	2.6	70	2.9	1.15
TiO_2	2.4	n.a.	5.9	2.0

[a] A surface with a higher surface acidity value is less likely to react with the pivalic acid; [b] Based on ref. [39]; [c] Based on ref. [40]; [d] IGZO = sputtered indium gallium zinc oxide.

oxidation state of MoCr at the surface is not known (especially after the O_2 plasma cleaning step) and because of the added complexity for multication metal oxides. According to both surface acidity scales, TiO_2 should have resulted in a lower nucleation delay, given the relatively high acidity. However, oxygen vacancies on TiO_2 have been reported to strongly influence its surface chemistry and to be responsible for chemisorption of carboxylic acid,[41,42] thus suggesting a need for caution when deriving trends from surface acidity scales that are calculated from the metal oxides formula. Yet, the exercise of considering surface acidity has already proven itself practical for designing area-selective ALD processes.[26,43] Furthermore, it is worth noting that the insertion of etch-back correction steps can in principle allow for further tuning of the selectivity. Depending on the "duty-cycle" during supercycle approach, i.e., depending on the ratio of etching to deposition cycles, one can potentially achieve selective deposition of SiO_2 on Ta_2O_5 and ZrO_2 but not on ZnO and IGZO, or alternatively have selective deposition on SiO_2, ZrO_2, Ta_2O_5 and not on IGZO, ZnO, and TiO_2. Such an approach can thus be very powerful when processing multimaterial surfaces.

2.3.5. Generalized Learnings

Better packing of pivalic acid effectively provides more steric hindrance than ethylbutyric acid with a longer chain, which in turn results into better inhibition as schematically depicted in **Figure 9**. Obviously, the packing and molecular size of SMIs should be compared to the size of the precursor that needs to be blocked and hence, precursors bulkier than BDEAS can in principle allow for longer nucleation delays also when using ethylbutyric acid as SMI. By comparing the results obtained in this work with those reported in the literature using acetylacetone as inhibitor,[26] an approximate linear relationship between the SMI size and the amount of nucleation delay is revealed (see **Table 5**). Smaller inhibitor molecules can in principle lead to higher surface densities.[44] However, we also show that not only the size but also the geometry of SMIs plays a key role in determining their effectiveness. In particular, both acetylacetone and ethylbutyric acid have a more linear molecular arrangement, while the chemisorbed pivalic acid creates a tertiary-butyl surface group which provides a better packing due to the smaller size and a more symmetric arrangement.
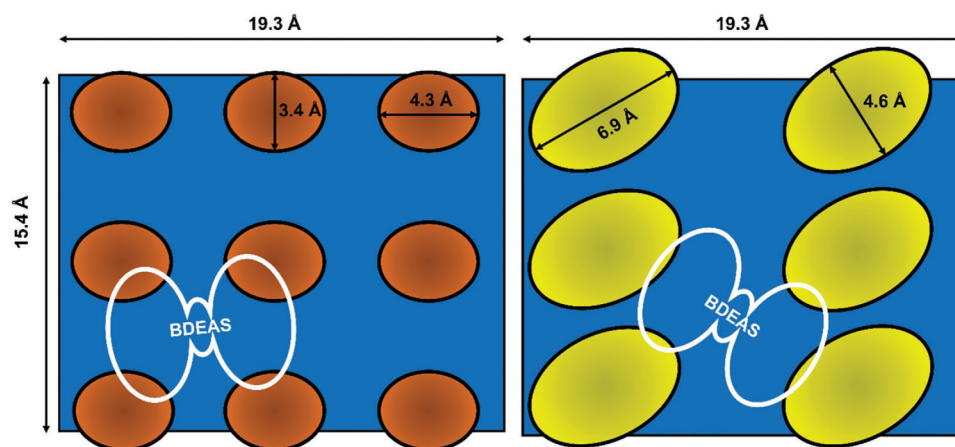

Figure 9. Schematic representation of 9 pivalic acid and 6 ethylbutyric acid inhibitor molecules bonded on a 19.3×15.4 Å^2 ZnO area as simulated by DFT, together with the size of a BDEAS precursor molecule in order to visualize the better steric shielding of the ZnO surface by the pivalic acid.

ADVANCED
SCIENCE NEWS
www.advancedsciencenews.com

ADVANCED
MATERIALS
www.advmat.de

Table 5. Three different SMIs binding on the ZnO surface for achieving area-selective ALD of SiO$_2$, together with the projected area they occupy on the surface when chemisorbed, their calculated chemisorption energies on ZnO and the estimated resulting ALD nucleation delays from spectroscopic ellipsometry data.

SMI on ZnO	Projected area of chemisorbed SMI [nm^2]	Binding energy on ZnO [eV]	SiO$_2$ nucleation delay [cycles]	Reference
Acetylacetone	≈0.45	1.3–1.47	≈5	[26,45]
Ethylbutyric acid	≈0.32	1.20–1.63	≈36	This work
Pivalic acid	≈0.15	1.82–2.17	≈70	This work

Furthermore, pivalic acid shows a higher chemisorption energy on ZnO than ethylbutyric acid, indicating a more stable chemisorbed inhibitor on the nongrowth area, which is less susceptible to being displaced.[34] As a matter of fact, pivalic acid is a known *protective group* in synthetic chemistry and is employed for that reason for screening-off hydroxyl groups and for selective functionalization of complex molecules. This way, many other suitable SMIs can therefore be selected from the literature on surface protective groups.

When interleaving etch-back correction steps, one needs to make sure that both growth and non-growth areas are virtually free from etching residues that can negatively affect the subsequent supercycle. Additional cleaning steps need to be considered as discussed in Sections 2.3.1 and 2.3.3. With respect to throughput, the use of atmospheric-pressure ALD allows for high partial pressures and therefore, higher doses, which effectively accelerates the saturation of the non-growth area with SMIs, thus enabling much shorter ALD cycle times. Similarly to the efforts undertaken in the literature on selective CVD,[12,13,46,47] further detailed research on, for example, the effect of processing conditions and reactor design needs to be carried out to highlight the advantages and limitations of the different configurations (e.g., throughput, loading effects, lateral overgrowth, etc.),[48] in correlation with the materials being investigated.

3. Conclusions

In this work we demonstrated atmospheric-pressure area-selective spatial ALD of SiO$_2$ using small molecule inhibitors (SMIs) in an ABC-type approach. Compared to a previously reported process using acetylacetate (Hacac), the use of more effective inhibition chemistries using ethylbutyric acid and pivalic acid results in ≈3–8 times larger selectivity for plasma enhanced ALD of SiO$_2$. At the same time, using ALD in spatial mode allows for up to ≈15 times faster deposition rates. For SiO$_2$ film growth the selectivity was further increased by interleaving newly developed spatial etch-back correction steps, using CF$_4$/O$_2$ plasma chemistry. Such atmospheric-pressure plasma etch process for SiO$_2$ was supercycled with an ABC-type spatial ALD process within the same tool, allowing for fully integrated spatial "*dep-etch*" processing of patterned wafers in a semi-automated mode. This way, up to 23.5 nm (using pivalic acid and conventional plasma etching) and ≈9.1 nm (integrated spatial ALD and etching) selective SiO$_2$ deposition was demonstrated.

The selectivity of both processes was studied by LEIS and XPS on large-area patterned samples, demonstrating their high selectivity and also providing insights into the role of supercycling back-etching correction steps. DFT calculations were employed to elucidate the surface chemistry underpinning the selective inhibition of the ZnO nongrowth area as a study case. It was shown that the selectivity of both carboxylic acid SMIs is thermodynamically controlled since the surface reactions on SiO$_2$ were found to be endothermic, while the reactions on the ZnO surface were exothermic. We further propose that pivalic acid is a better inhibitor than ethylbutyric acid due to its capability of better packing, enabling a more effective steric shielding of the surface against the subsequent precursor adsorption. In addition, we applied the selective deposition process to surfaces with materials other than ZnO that can be used as possible growth and nongrowth areas in functional devices. We also note that the etch-back correction steps can be used as an additional process parameter for tuning the selectivity between growth and nongrowth areas. This novel approach demonstrates a vast potential in novel device and cost-effective thin-film manufacturing.

We show that extra care should be taken when designing such processes in terms of the composition of the surface following the etch-back steps. In particular, surface contamination by etchants may affect the efficiency of the subsequent supercycles and inhibitor binding, therefore it calls for countermeasures to reset the surfaces to their initial state in order to maintain high-selectivity and low variability from supercycle to supercycle.

Besides representing a first-of-its-kind in many aspects, we believe that the results presented in this work are an important step for further understanding the use of SMIs together with interleaved etching steps to achieve high selectivity. To this end, we describe generalized learnings that will help developing ever more effective strategies for highly selective ASD processes relying on SMIs.

4. Experimental Section

ALD Processes: Depositions were carried out in an home-built rotary spatial ALD reactor, which is described in detail in ref. [49]. In short, it consists of a rotating substrate holder that can accommodate 150-mm wafers and an injector head with several slots for gas-phase reactants delivery, separated by inert N$_2$ curtains. The reactor is enclosed in a convective oven for temperature control and under atmospheric pressure. The exposure to each reactants is set by the partial pressure of the reactant and the rotation speed expressed in rotations-per-minute, RPM. The injector head is equipped with a dielectric barrier discharge (DBD) plasma source. For the ZnO deposition, diethylzinc was used as the precursor and water as the coreactant. 200 spatial ALD cycles were ran at 30 RPM, resulting in ≈26 nm thick ZnO layers. Large area ZnO patterns (≈3 × 3 cm^2) were defined using a resist-ink pen (with CIF Black Etch Resist). The areas free of the resist areas were then etched using a 5% oxalic acid solution (2 minutes). The resist was then removed by successive cleaning steps with acetone, ethanol and water, and the wafer was N$_2$ blow-dried. For the ABC-type

**ADVANCED
SCIENCE NEWS**

www.advancedsciencenews.com

**ADVANCED
MATERIALS**

www.advmat.de

SiO_2 plasma-assisted spatial ALD, two inhibitors were tested: ethylbutyric acid (99%; CAS number 88-09-5) and trimethylacetic acid also known as pivalic acid, (99%; CAS number 75-98-9). Bis(diethylamino)silane, BDEAS ($H_2Si[N(C_2H_5)_2]_2$), was used as the silicon precursor and a mixture of 1% O_2 in N_2 as the DBD plasma feeding gas coreactant. The inhibitors ethylbutyric acid and pivalic acid were from Sigma-Aldrich and used without further purification. Both carboxylic acids were held in glass bubblers held at 75 and 60 °C, respectively, to ensure high vapor pressure. An Ar bubbling flow of 500 sccm was used to transport the vapor, further diluted with additional 200 sccm of Ar before reaching the injector head. BDEAS was stored in a stainless steel bubbler and kept at room temperature (vapor pressure 1.1 Torr at 22 °C). Bubbling Ar flows of 50 sccm at 10 and 20 RPM and 100 sccm at 30 RPM were used to carry the vapor to the injector head. The flow was further diluted with Ar to a total of 1000 sccm before reaching the reactor. 100 sccm of O_2 were supplied to the DBD plasma source with a frequency of 65 kHz and a supply voltage of 120 V. A rotation speed of 20 RPM was used for all experiments with ethylbutyric acid; 10 RPM or 30 RPM (only in the latter case the bubbler temperature was set to 80 °C) with pivalic acid. Based on the vapor pressure data for both pivalic and ethylbutyric acid,[50] a comparable total exposure for all three settings is estimated, varying from 2 to 3 Torr. Exposures above 2 Torr were necessary to achieve the highest selectivity during the process development phase. All experiments were carried out at a substrate temperature of 100 °C. Prior to deposition, 20 cycles of O_2 plasma were used as a cleaning step, followed by 20 cycles of inhibitor dosing, to ensure the entire substrate wafer was initially saturated with the inhibitor.

Plasma Etching Process: Proof-of-principle experiments using supercycles with conventional plasma etching were conducted moving substrates from the spatial ALD tool to a reactive ion etcher from (PSC Plasma Etch Reactor III, E 3070 by Polyteknik) with a $CF_4 + O_2$ feeding gas.

All other etching experiments were performed in the same spatial ALD rotary reactor as described above. CF_4, O_2 and N_2 were transported through separate gas lines to the plasma source from a centralized gas supply and merged only at about 50 cm upstream of the plasma source. Each line has individual mass flow controllers and manual valves. 150-mm c-Si wafers with 325 nm thick thermally grown SiO_2 were used as starting substrates for the etching experiments. Both *static mode*, i.e., no substrate rotation underneath the injector head, and *dynamic mode*, i.e., with wafer rotation were explored for the etching experiments.

Analytical Methods: An ex situ Horiba Uvisel 2 spectroscopic ellipsometer was used to measure the thickness of the spatial ALD deposited layers and of the SiO_2 layers before and after each etching experiment. Ellipsometric data were acquired from 1.5 to 3.5 eV with steps of 0.1 eV and 500 ms integration time. The spectroscopic ellipsometry measurements were acquired at an incidence angle of 70° a spot size of 2030 × 705 µm^2 and a modulator—analyzer configuration of 0°–45°. For each radial position on the wafer 4 different locations were measured using an automated mapping recipe. The so-collected data were used to calculate an averaged etch rate.

XPS measurements were performed using a Quantera Hybrid from ULVAC-PHI with a monochromatic Al Kα-radiation and a take-off angle of 45°. Low energy ion scattering spectroscopy measurements were taken using a LEIS, Qtac^{100} system from IONTOF GmbH, using 3 keV ^{4}He$^+$ for overview spectra and 6–8 keV ^{4}He$^+$ for SiO_2 layer thickness measurements. In situ generated atomic oxygen was employed to clean the surfaces prior to analysis.

Computational Methodology: All electronic structure calculations were performed with the projector augmented wave function (PAW)[51,52] formalism, as implemented in the Vienna Ab Initio Simulation Package (VASP v. 5.4.4).[53–55] Periodic Density Functional Theory (DFT) calculations were carried out within the Generalized Gradient Approximation (GGA)[56,57] jointly with the Perdew—Burke—Ernzerhof (PBE)[58] [8] exchange-correlation functional. Long-range Van der Waals interactions were included on an empirical basis (PBE-D3).[59] For an accurate electronic description of the strongly correlated Zn-3d orbitals, we applied the GGA+U scheme of Dudarev et al.[60] with the effective Hubbard U parameter ($U_{eff} = U - J$) being set to 7.5 eV based on previous ZnO studies.[32,61] In all calculations, a Gaussian smearing of 0.1 eV was used, and the con-

vergence tolerance for the self-consistent electronic minimization was set to 10^{-8} eV cycle^{-1}. Otherwise, "normal" precision settings were adopted.

To accommodate the bulky ethylbutyric acid and pivalic acid inhibitors and minimize the spurious interactions between periodic images, simulation unit cells were kept rather large in the *xy*-plane, on which substrates are aligned (see Figure S15 in the Supporting Information for the exact model systems). Similarly, all model systems contained a vacuum padding of at least 12 Å, ensuring a sufficient separation between two consecutive surface slabs. Structural relaxations were carried out using the conjugate gradient (CG) algorithm, where they were considered converged once all forces deviate less than 0.05 eV Å^{-1} in two consecutive ionic steps. Each surface slab model (without inhibitors) was preoptimized with a plane-wave basis-set cutoff energy of 520 eV and 4×4×1 Monkhorst–Pack (MP) K-point grid (including the Γ-point), whereby all cell parameters were fully relaxed along with the geometry. These were followed by the geometry-only (fixed cell) optimizations for the surface models also including the inhibitor(s) adsorbed on a given surface. Due to the large size of the surface slab models with adsorbates, only the Γ-point was considered (allowing for the use of the faster Γ-only implementation of VASP) along with a smaller plane-wave cut-off energy (400 eV). Otherwise all other DFT settings were kept identical.

Minimum energy pathways (MEPs) along the predefined reaction coordinates describing the chemisorption of an ethylbutyric acid/pivalic acid inhibitor molecule on ZnO (bare and hydrogenated) and SiO_2 surfaces were computed using the climbing-image nudge elastic band (CI-NEB) method,[62] as implemented in VASP VTST tools (v. 940).[63] CI-NEB optimizations were done with a looser convergence criterion on forces (0.1 eV Å^{-1}) utilizing the Hessian-based (G)-LBFGS and FIRE algorithms as implemented in VTST tool set.[64,65] Depending on the distance between the initial and final states (structures) along the collective reaction coordinate for a given minimum-energy pathway, five or more interconnected images were considered in the NEB calculations, aiming to maintain a distance of maximum 0.4 Å between two consecutive images.

For investigating the thermal stability of the hydrogenated ZnO (ZnO:H) surface models considered here, a simulated annealing procedure based on ab initio molecular dynamics (AIMD) simulations is used. In this approach, a temperature ramp (i.e., gradual heating) from 300 K to a high final temperature, 1200 K, is simulated. This process consists of a series of microcanonical (NVE) ensembles of 100 fs (totaling to 5 ps) with initial temperatures set to the interval temperature at a given gradual heating step. It is noted that this approach is likely to predict thermal processes to occur at higher temperatures than in reality. This is essentially due to fact that the simulated system is heated more rapidly (in the picoseconds domain), thus it is not given enough time to equilibrate as opposed to the experiments, where heating is at the macroscopic scale (seconds domain). However, such rapid heating is unavoidable due to computational limitations, and it is sufficiently suitable for quick qualitative comparisons of the thermal phenomena under investigation.

Selection of the Model Systems: Describing the substrate surfaces using a realistic model is vital in obtaining reliable first-principles adsorption energetics. Through a detailed DFT analysis on the stability of different Wurtzite ZnO orientations, ZnO($10\bar{1}0$) was predicted to be most stable surface,[32] which is supported by the X-ray diffraction (XRD) data taken for the ZnO films deposited at typical ALD temperatures ($T = 23$–80 °C).[66] Therefore ZnO($10\bar{1}0$) surface models were adopted in the DFT simulations (see Figure S15 in the Supporting Information). Starting from the hexagonal ZnO bulk structure ($P6_3mc$, Materials Project Database ID: mp-2133), a 5 × 3 × {4/6} supercell of the ($10\bar{1}0$) termination, with the dimensions of 16.3 Å × 15.6 Å × {39.4/45.0} Å (including the vacuum padding) was created. The surface formation and adsorption energies (of a pivalic acid inhibitor in the same orientation) using the 4-layer and 6-layer models were compared. As the energies vary only less than 30 meV (per atom) in going from 4 to 6 layers, the 4-layer ZnO model was chosen in the following calculations to limit the computational efforts.

As for modeling the SiO_2 substrate surface, a hydroxylated version of the reconstructed α-SiO_2 (0001) model (viz. SiO_2:H, see Figure S15 in the Supporting Information) was generated,[67] variants of which were also used in studying similar ALD precursor adsorption processes.[19,26,68,69]

Starting from the hexagonal SiO_2 phase ($P6_322$, MP-ID: mp-559091), the 4×4 supercell, containing 6 layers, with dimensions of 19.4 Å × 19.4 Å × 30.3 Å was generated. In addition, ethylbutyric acid and pivalic acid inhibitor molecules (Figure S14, Supporting Information) were used to simulate their binding on different ZnO and SiO_2 surfaces. To obtain compatible reference energies, isolated inhibitor molecules were simulated in periodic boxes with 15 Å padding in each direction using the same DFT settings as surfaces.

Ab Initio Energetics Calculations for Inhibitor Adsorption: Binding (or equivalently adsorption) energy (E_{bind}) for a given adsorbate, either an inhibitor (ethylbutyric acid/pivalic acid molecule) or an H_2 molecule is calculated as

$$E_{bind} = \left(E_{comp} - E_{surf} - N_{ads} \times E_{ads} \right) / N_{ads} \tag{1}$$

where E_{comp} is the total energy of the surface-adsorbate complex, E_{surf} the energy of the surface slab (bare/hydrogenated ZnO or hydroxylated SiO_2), E_{ads} the energy of the isolated adsorbate and N_{ads} the number of adsorbates binding simultaneously on the surface. Here, two distinct types of binding modes can be defined, i.e., physisorption (molecular binding) versus chemisorption (dissociative binding). A strong chemisorption is often required for the adsorbate to stick on the surface through the subsequent purging cycle, while a strong physisorption is key in increasing the probability of the adsorbate to undergo dissociative reactions (chemisorption). To probe the inhibitor adsorption thermodynamics, a reaction energy for the conversion of physisorbed species into the chemisorbed one through dissociation reactions was defined as

$$\varepsilon E_r = \varepsilon E_c - \varepsilon E_p \tag{2}$$

where ΔE_c and ΔE_p are the chemisorption and physisorption energies. In contrast, the kinetics aspects were studied through the energy barriers extracted from the calculated MEPs. All reported energies correspond to 0 K calculations.

Supporting Information

Supporting Information is available from the Wiley Online Library or from the author.

Conflict of Interest

F.R. and A.M. declare the following competing financial interest(s): a patent application partly based on this work has been filed as WO2021096359A1 on May 20, 2021.

Data Availability Statement

The data that support the findings of this study are available from the corresponding author upon reasonable request.

[1] K. Cao, J. Cai, X. Liu, R. Chen, *J. Vac. Sci. Technol. A: Vacuum, Surfaces, Film* **2018**, *36*, 010801.
[2] N. Cheng, M. N. Banis, J. Liu, A. Riese, X. Li, R. Li, S. Ye, S. Knights, X. Sun, *Adv. Mater.* **2015**, *27*, 277.
[3] R. Li, F. Zhang, D. Wang, J. Yang, M. Li, J. Zhu, X. Zhou, H. Han, C. Li, *Nat. Commun.* **2013**, *4*, 1432.
[4] N. M. Miskovsky, P. H. Cutler, A. Mayer, B. L. Weiss, B. Willis, T. E. Sullivan, P. B. Lerner, *J. Nanotechnol.* **2012**, *2012*, 512379.
[5] H. P. Chen, Y. H. Wu, H. Y. Huang, C. H. Tsai, S. K. Lee, C. C. Lee, T. H. Wei, H. C. Yao, Y. C. Wang, C. Y. Liao, H. K. Chang, C. W. Lu, W. S. Shue, M. Cao, in *Proceedings of the 2021 IEEE International Electron Devices Meeting (IEDM)*, San Francisco, CA, 11–16 December 2021, (IEEE, New York, 2021), **2021**, 2021-Decem, 2211.
[6] T. H. Cho, N. Farjam, C. R. Allemang, C. P. Pannier, E. Kazyak, C. Huber, M. Rose, O. Trejo, R. L. Peterson, K. Barton, N. P. Dasgupta, *ACS Nano* **2020**, *14*, 17262.
[7] R. Chen, S. F. Bent, *Adv. Mater.* **2006**, *18*, 1086.
[8] B. D. Joyce, J. A. Baldrey, *Nature* **1962**, *195*, 485.
[9] J. G. Fleming, T. R. Omstead, F. Dominguez, in *Adv. Met. ULSI Appl*, (Eds: V. V. S. Rana, R. V. Joshi, I. Ohdomari), Materials Research Society, Pittsburgh **1992**, p. 233.
[10] S. M. Gates, *Chem. Rev.* **1996**, *96*, 1519.
[11] P. Mårtensson, J.-O. Carlsson, *J. Electrochem. Soc.* **1998**, *145*, 2926.
[12] J. O. Carlsson, M. Boman, *J. Vac. Sci. Technol. A: Vacuum, Surfaces, Film* **1985**, *3*, 2298.
[13] J. O. Carlsson, *Crit. Rev. Solid State Mater. Sci.* **1990**, *16*, 161.
[14] S. Kannan Selvaraj, J. Parulekar, C. G. Takoudis, *J. Vac. Sci. Technol. A: Vacuum, Surfaces, Film.* **2014**, *32*, 010601.
[15] C. T. Nguyen, E. H. Cho, B. Gu, S. Lee, H. S. Kim, J. Park, N. K. Yu, S. Shin, B. Shong, J. Y. Lee, H. B. R. Lee, *Nat. Commun.* **2022**, *13*, 7597.
[16] G. N. Parsons, R. D. Clark, *Chem. Mater.* **2020**, *32*, 4920.
[17] K. J. Hughes, J. R. Engstrom, *J. Vac. Sci. Technol. A: Vacuum, Surfaces, Film.* **2012**, *30*, 01A102.
[18] R. W. Johnson, A. Hultqvist, S. F. Bent, *Mater. Today* **2014**, *17*, 236.
[19] A. Mameli, Y. Kuang, M. Aghaee, C. K. Ande, B. Karasulu, M. Creatore, A. J. M. Mackus, W. M. M. Kessels, F. Roozeboom, *Chem. Mater.* **2017**, *29*, 921.
[20] T. Suh, Y. Yang, H. W. Sohn, R. A. DiStasio, J. R. Engstrom, *J. Vac. Sci. Technol. A* **2020**, *38*, 062411.
[21] S. E. Atanasov, B. Kalanyan, G. N. Parsons, *J. Vac. Sci. Technol. A: Vacuum, Surfaces, Film.* **2016**, *34*, 01A148.
[22] B. Kalanyan, P. C. Lemaire, S. E. Atanasov, M. J. Ritz, G. N. Parsons, *Chem. Mater.* **2016**, *28*, 117.
[23] D. Bobb-Semple, K. L. Nardi, N. Draeger, D. M. Hausmann, S. F. Bent, *Chem. Mater.* **2019**, *31*, 1635.
[24] I. Zyulkov, M. Krishtab, S. De Gendt, S. Armini, *ACS Appl. Mater. Interfaces* **2017**, *9*, 31031.
[25] J. Soethoudt, Y. Tomczak, B. Meynaerts, B. T. Chan, A. Delabie, *J. Phys. Chem. C* **2020**, *124*, 7163.
[26] A. Mameli, M. J. M. Merkx, B. Karasulu, F. Roozeboom, W. M. M. Kessels, A. J. M. Mackus, *ACS Nano* **2017**, *11*, 9303.

**ADVANCED
SCIENCE NEWS**

www.advancedsciencenews.com

**ADVANCED
MATERIALS**

www.advmat.de

[27] T. Suh, Y. Yang, P. Zhao, K. U. Lao, H. Y. Ko, J. Wong, R. A. Distasio, J. R. Engstrom, *ACS Appl. Mater. Interfaces* **2020**, *12*, 9989.

[28] R. Vallat, R. Gassilloud, B. Eychenne, C. Vallée, *J. Vac. Sci. Technol. A: Vac. Surf., Film.* **2017**, *35*, 01B104.

[29] M. Fang, J. C. Ho, *ACS Nano* **2015**, *9*, 8651.

[30] M. J. M. Merkx, S. Vlaanderen, T. Faraz, M. A. Verheijen, W. M. M. Kessels, A. J. M. Mackus, *Chem. Mater.* **2020**, *32*, 7788.

[31] R. Khan, B. Shong, B. G. Ko, J. K. Lee, H. Lee, J. Y. Park, I. K. Oh, S. S. Raya, H. M. Hong, K. B. Chung, E. J. Luber, Y. S. Kim, C. H. Lee, W. H. Kim, H. B. R. Lee, *Chem. Mater.* **2018**, *30*, 7603.

[32] Q. L. Tang, Q. H. Luo, *J. Phys. Chem. C* **2013**, *117*, 22954.

[33] L. T. Zhuravlev, *Colloids Surf. A: Physicochem. Eng. Asp.* **2000**, *173*, 1.

[34] H. Kung, A. Teplyakov, *J. Phys.: Condens. Matter* **2015**, *27*, 054007.

[35] C. J. Mogab, A. C. Adams, D. L. Flamm, *J. Appl. Phys.* **1978**, *49*, 3796.

[36] R. D'Agostino, F. Cramarossa, S. De Benedictis, G. Ferraro, *J. Appl. Phys.* **1981**, *52*, 1259.

[37] D. L. Flamm, C. J. Mogab, E. R. Sklaver, *J. Appl. Phys.* **1979**, *50*, 6211.

[38] V. M. Donnelly, A. Kornblit, *J. Vac. Sci. Technol. A: Vac., Surf., Film.* **2013**, *31*, 050825.

[39] A. Auroux, A. Gervasini, *J. Phys. Chem.* **1990**, *94*, 6371.

[40] N. C. Jeong, J. S. Lee, E. L. Tae, Y. J. Lee, K. B. Yoon, *Angew. Chem. Int. Ed.* **2008**, *47*, 10128.

[41] M. Buchholz, M. Xu, H. Noei, P. Weidler, A. Nefedov, K. Fink, Y. Wang, C. Wöll, *Surf. Sci.* **2016**, *643*, 117.

[42] L. Ojamäe, C. Aulin, H. Pedersen, P. O. Käll, *J. Colloid Interface Sci.* **2006**, *296*, 71.

[43] C. Zhang, E. Tois, M. Leskelä, M. Ritala, *Chem. Mater.* **2022**, *34*, 8379.

[44] J. Li, I. Tezsevin, M. J. M. Merkx, J. F. W. Maas, W. M. M. Kessels, T. E. Sandoval, A. J. M. Mackus, *J. Vac. Sci. Technol. A* **2022**, *40*, 062409.

[45] T. L. Bahers, T. Pauporté, F. Labat, G. Lefèvre, I. Ciofini, *Langmuir* **2011**, *27*, 3442.

[46] M. Kastelic, I. Oh, C. G. Takoudis, J. A. Friedrich, G. W. Neudeck, *Chem. Eng. Sci.* **1988**, *43*, 2031.

[47] J. O. Carlsson, *JVSTA* **1988**, *6*, 1656.

[48] W. S. Cheong, *ETRI J.* **2003**, *25*, 503.

[49] A. Illiberi, R. Scherpenborg, F. Roozeboom, P. Poodt, *ECS J. Solid State Sci. Technol.* **2014**, *3*, P111.

[50] National Institute of Standards and Technology, in *Chem. WebBook, NIST Stand. Ref. Database Number 69*, Natl. Inst. Stand. Technol. (Eds: P.J. Linstrom, W.G. Mallard), Gaithersburg MD 20899.

[51] P. E. Blöchl, *Phys. Rev. B* **1994**, *50*, 17953.

[52] G. Kresse, *Phys. Rev. B* **1999**, *59*, 1758.

[53] G. Kresse, J. Hafner, *Phys. Rev. B* **1993**, *47*, 558.

[54] G. Kresse, J. Hafner, *Phys. Rev. B* **1994**, *49*, 14251.

[55] G. Kresse, J. Furthmüller, *Comput. Mater. Sci.* **1996**, *6*, 15.

[56] P. Hohenberg, *Phys. Rev.* **1964**, *136*, B864.

[57] W. Kohn, L. J. Sham, *Phys. Rev.* **1965**, *140*, A1133.

[58] J. P. Perdew, K. Burke, M. Ernzerhof, *Phys. Rev. Lett.* **1997**, *78*, 1396.

[59] S. Grimme, J. Antony, S. Ehrlich, H. Krieg, *J. Chem. Phys.* **2010**, *132*, 154104.

[60] S. Dudarev, G. Botton, *Phys. Rev. B: Condens. Matter Mater. Phys.* **1998**, *57*, 1505.

[61] P. Erhart, K. Albe, A. Klein, *Phys. Rev. B: Condens. Matter Mater. Phys.* **2006**, *73*, 205203.

[62] G. Henkelman, B. P. Uberuaga, H. Jónsson, *J. Chem. Phys.* **2000**, *113*, 9901.

[63] VTST tool set for VASP, **n.d.**

[64] J. Nocedal, *Math. Comput.* **1980**, *35*, 773.

[65] E. Bitzek, P. Koskinen, F. Gähler, M. Moseler, P. Gumbsch, *Phys. Rev. Lett.* **2006**, *97*, 170201.

[66] J. Cai, Z. Ma, U. Wejinya, M. Zou, Y. Liu, H. Zhou, X. Meng, *J. Mater. Sci.* **2019**, *54*, 5236.

[67] O. I. Malyi, V. V. Kulish, C. Persson, *RSC Adv.* **2014**, *4*, 55599.

[68] A. Mameli, B. Karasulu, M. A. Verheijen, B. Barcones, B. Macco, A. J. M. Mackus, W. M. M. E. Kessels, F. Roozeboom, *Chem. Mater.* **2019**, *31*, 1250.

[69] M. Shirazi, W. M. M. Kessels, A. A. Bol, *Phys. Chem. Chem. Phys.* **2018**, *20*, 16861.